Statistics of turbulence and intermittency enhancement in superfluid ^{4}He counterflow

S. Bao,[1,2] W. Guo,[1,2] V. S. L'vov,[3] and A. Pomyalov[3]

[1]*National High Magnetic Field Laboratory, 1800 East Paul Dirac Drive, Tallahassee, Florida 32310, USA*
[2]*Mechanical Engineering Department, Florida State University, Tallahassee, Florida 32310, USA*
[3]*Department of Chemical and Biological Physics, Weizmann Institute of Science, Rehovot 76100, Israel*

We report a detailed analysis of the energy spectra, second- and high-order structure functions of velocity differences in superfluid ^{4}He counterflow turbulence, measured in a wide range of temperatures and heat fluxes. We show that the one-dimensional energy spectrum $E_{xz}(k_y)$ (averaged over the xz plane, parallel to the channel wall), directly measured as a function of the wall-normal wave vector k_y, gives more detailed information on the energy distribution over scales than the corresponding second-order structure function $S_2(\delta_y)$. In particular, we discover two intervals of k_y with different apparent exponents: $E_{xz}(k_y) \propto k_y^{-m_C}$ for $k \lesssim k_\times$ and $E_{xz}(k_y) \propto k_y^{-m_F}$ for $k \gtrsim k_\times$. Here $k_\times$ denotes the wave number that separates scales with relatively strong (for $k \lesssim k_\times$) and relatively weak (for $k \gtrsim k_\times$) coupling between the normal-fluid and superfluid velocity components. We interpret these k ranges as *cascade-dominated* and *mutual-friction-dominated* intervals, respectively. The general behavior of the experimental spectra $E_{xz}(k_y)$ agrees well with the predicted spectra [L'vov and Pomyalov, [Phys. Rev. B **97**, 214513 (2018)](#)]. Analysis of the nth-order structure functions statistics shows that in the energy-containing interval, the statistics of counterflow turbulence is close to Gaussian, similar to the classical hydrodynamic turbulence. In the cascade- and mutual-friction-dominated intervals, we found some modest enhancement of intermittency with respect to its level in classical turbulence. However, at small scales, the intermittency becomes much stronger than in the classical turbulence.

I. INTRODUCTION

Below the Bose-Einstein condensation temperature $T_\lambda \approx$ 2.17 K, liquid ^{4}He becomes a quantum superfluid [1–3] with the vorticity constrained to vortex-line singularities of core radius $a_0 \approx 10^{-8}$ cm and fixed circulation $\kappa = h/M$ [4]. Here, h is Planck's constant and M is the mass of the ^{4}He atom. The superfluid turbulence is manifested as a complex tangle of these vortex lines with a typical intervortex distance $\ell \sim 10^{-4}$–10^{-2} cm [5].

Large-scale hydrodynamics of such system is usually described by a two-fluid model, interpreting ^{4}He as a mixture of two coupled fluid components: an inviscid superfluid and a viscous normal fluid. The temperature-dependent densities of the components $\rho_s(T)$ and $\rho_n(T)$ define their contributions to the mixture. The total density of ^{4}He $\rho = \rho_s(T) + \rho_n(T) = \rho(T)$ weakly depends on the temperature. The tangle of quantum vortices mediates the interaction between fluid components via mutual-friction force [2,5–8].

There is a building evidence [9–12] that the large-scale turbulence in mechanically driven superfluid ^{4}He is similar to the classical turbulence. In this case, both components move with close velocities being coupled by the mutual-friction force at almost all scales. On the contrary, the turbulence generated in superfluid ^{4}He by a heat flux in a channel has no classical analogy. Here the two components move in the opposite directions relative to the channel walls, with respective mean velocities $\boldsymbol{U}_n$ and $\boldsymbol{U}_s$. In this way, the counterflow velocity $\boldsymbol{U}_{ns} = \boldsymbol{U}_n - \boldsymbol{U}_s \neq 0$, proportional to the applied heat flux, is created along the channel. When U_{ns} is above some

small critical velocity, it can trigger the creation of a tangle of vortex lines.

Systematic experimental studies of counterflow turbulence, pioneered by classical 1957 papers of Vinen [7], usually concentrated mostly on global characteristics of the vortex tangle; cf. Ref. [12] for a review. The statistics of turbulent fluctuations was not accessible. Recently, the turbulent statistics in the ^{4}He normal component was measured in the form of the cross-stream second-order structure functions [13,14],

$$S_2(Y) = \langle |\Delta u_x(Y, y, t)|^2 \rangle. \quad (1a)$$

Here, $\langle \cdot \rangle$ denotes an ensemble average over many trials and $\Delta u_x(Y, y, t)$ is the streamwise velocity difference,

$$\Delta u_x(Y, y, t) = u_x(y + Y, t) - u_x(y, t). \quad (1b)$$

Other studies [15,16] measured the statistics of the superfluid component.

Recent theoretical analysis [17] found that the energy spectra in counterflow turbulence are not scale invariant and cannot be rigorously connected with apparent scaling exponents of the second-order velocity structure functions measured in Ref. [13] at modest values of the Reynolds numbers. In this paper, we suggest an alternative way to analyze the visualization data [13] that allows the one-dimensional energy spectra to be determined so that a direct comparison with theoretical predictions [17] can be made. In addition, we use higher-order structure functions to assess the level of intermittency in counterflow turbulence.

The paper is organized as follows. The analytical background of the problem of statistical description of superfluid counterflow turbulence is covered in Sec. II. It starts with Sec. II A, which is devoted to the second-order statistical characteristics of homogeneous turbulence. In Sec. II B, we suggest a method of velocity data analysis that allows one to directly extract the one-dimensional energy spectra. The recent analytic theory of counterflow turbulence [17], required for our current analysis, is summarized in Sec. II C. The main result of the theory is the energy balance given by Eq. (9) that allows one to find the normal-fluid and superfluid energy spectra in a wide range of the problem parameters.

Our experimental results on the statistics of the normal-fluid turbulence and their analysis are presented in Sec. III. In Sec. III A, we briefly describe the experimental techniques. The important crossover wave numbers for the current problem are estimated in Sec. III B. Section III C is devoted to the second-order statistics of counterflow turbulence: the velocity structure functions $S_2(\delta)$ (see Sec. III C 1 and left column of Fig. 1) and the energy spectra $E(k)$ (see Sec. III C 2 and middle column of Fig. 1). In particular, we demonstrate that the counterflow energy spectra can be divided in two subintervals: a cascade-dominated interval and a mutual-friction-dominated interval, with the apparent scaling exponents $m_c \simeq 2$ and $m_F \simeq 3$ (see Fig. 1, right column). An important question about the relationship between $S_2(\delta)$ and $E(k)$ is discussed in Sec. III C 3 and illustrated in Fig. 2. We show in Sec. III D and Fig. 3 that the theoretically predicted energy spectra are in good agreement with the experimental energy spectra in the cascade-dominated range of wave numbers.

In Sec. III E, we concentrate on high-order velocity structure functions,

$$S_4(Y) = \langle |\Delta u_x(Y, y, t)|^4 \rangle, \quad S_6(Y) = \langle |\Delta u_x(Y, y, t)|^6 \rangle.$$
(1c)

In Fig. 4, we show that the flatness $F_4(Y)$ and hyperflatness $F_6(Y)$,

$$F_4(Y) = S_4(Y)/S_2^2(Y), \quad F_6(Y) = S_6(Y)/S_2^3(Y),$$
(2)

have two ranges of power-law behavior with an apparent scaling of $F_4(Y) \propto Y^{x_4^{(1),(2)}}$ and $F_6(Y) = \propto Y^{x_6^{(1),(2)}}$, respectively. For Y larger than some Y_* that corresponds to the cascade- and mutual-friction-dominated subintervals of the energy spectra, $x_4^{(1)} \simeq 0.20$ and $x_6^{(1)} \simeq 0.50$, which are moderately larger than the inertial range exponents in classical hydrodynamic turbulence, i.e., $x_4^{HT} \simeq 0.14$ and $x_6^{HT} \simeq 0.38$. However, as Y approaches the viscous scales (i.e., $Y \lesssim Y_*$), the small-scale intermittency becomes stronger: $x_4^{(2)} \simeq 0.5$ and $x_6^{(2)} \simeq 1.4$. This behavior is similar to the intermittency enhancement observed in the mechanically driven ^{4}He [18,19].

Finally, Sec. IV briefly summarizes our findings.

II. ANALYTICAL BACKGROUND

A. Second-order statistical characteristics of homogeneous superfluid turbulence

The most general statistical description of the homogeneous superfluid ^{4}He turbulent velocity field $\boldsymbol{u}_j(\boldsymbol{r})$ at the level of the second-order statistics can be done in terms of

the three-dimensional (3D) cross-correlation functions of the normal-fluid and superfluid turbulent velocity fluctuations in the $\boldsymbol{k}$ representation,

$$(2\pi)^3 \delta(\boldsymbol{k} + \boldsymbol{k}') F_{ij}^{\alpha\beta}(\boldsymbol{k}) = \langle v_i^\alpha(\boldsymbol{k}) v_j^\beta(\boldsymbol{k}') \rangle.$$
(3a)

Here, $\boldsymbol{v}_j(\boldsymbol{k})$ is the Fourier transform of $\boldsymbol{u}_j(\boldsymbol{r})$,

$$\boldsymbol{v}_i(\boldsymbol{k}) = \int \boldsymbol{u}_i(\boldsymbol{r}) \exp(i\boldsymbol{k} \cdot \boldsymbol{r}) \, d\boldsymbol{r},$$
(3b)

$F_j(\boldsymbol{k}) \equiv F_j^{\alpha\alpha}(\boldsymbol{k})$, $\alpha, \beta = \{x, y, z\}$ are vector indexes, subscripts "$_{i,j}$" denote the normal-fluid ($i, j = $ n) or the superfluid ($i, j = $ s) components, and $\boldsymbol{k}$ is the wave vector. The inverse Fourier transform is defined as follows:

$$\boldsymbol{u}_i(\boldsymbol{r}) = \int \boldsymbol{v}_i(\boldsymbol{k}) \exp(-i\boldsymbol{k} \cdot \boldsymbol{r}) \frac{d\boldsymbol{k}}{(2\pi)^3}.$$
(3c)

The visualization technique, to be discussed in more detail in Sec. III A, allows one to measure the streamwise normal-fluid velocity across a channel, $v_n^x(y, t)$. Henceforth, unless stated explicitly, we consider only this velocity component, i.e., $i, j = $ n, $\alpha = \beta = x$, and omit these indexes. For example, $F_{ij}^{\alpha\beta}(\boldsymbol{k}) \Rightarrow F_{nn}^{xx}(\boldsymbol{k}) \Rightarrow F(\boldsymbol{k})$.

More compact, but less detailed information on the statistics of turbulence is given by one-dimensional (1D) energy spectra $E(k)$ averaged over all directions of vector $\boldsymbol{k}$,

$$E_{sp}(k) = \frac{k^2}{(2\pi)^3} \int F(\boldsymbol{k}) d\cos\theta \, d\varphi.$$
(4a)

Here we used spherical coordinates, with polar and azimuth angles θ and φ. The polar angle is measured from the direction of $\boldsymbol{U}_{ns}$.

In the isotropic case, $F(\boldsymbol{k}) = F(k)$, i.e., is independent of θ and φ. Thus,

$$E_{sp}(k) = \frac{k^2}{2\pi^2} F(k) \quad \text{for spherical symmetry.}$$
(4b)

Some information about possible anisotropy of the second-order statistics of turbulence can be obtained by comparison of the 1D (spherically averaged) function $E_{sp}(k)$, with the 1D functions $E_{xy}(k_z)$, $E_{zx}(k_y)$, and $E_{yz}(k_x)$ averaged over the xy, zx, and yz planes. These functions depend only on the projections of $\boldsymbol{k}$, orthogonal to the corresponding planes. Understanding $F(\boldsymbol{k})$ in the Cartesian coordinates as $F(k_x, k_y, k_z)$, we define

$$E_{xy}(k_z) = \int F(k_x, k_y, k_z) \frac{dk_x \, dk_y}{4\pi^2},$$

$$E_{zx}(k_y) = \int F(k_x, k_y, k_z) \frac{dk_x \, dk_z}{4\pi^2},$$

$$E_{yz}(k_x) = \int F(k_x, k_y, k_z) \frac{dk_y \, dk_z}{4\pi^2}.$$
(4c)

The total kinetic energy E of the system can be found by respective integration,

$$E = \int E_{sp}(k) \frac{dk}{2\pi} = \int E_{xy}(k_z) \frac{dk_z}{2\pi} = \cdots.$$
(5)

In the case of spherical symmetry, all four 1D functions given by Eq. (4b) and Eq. (4c) are proportional to each other
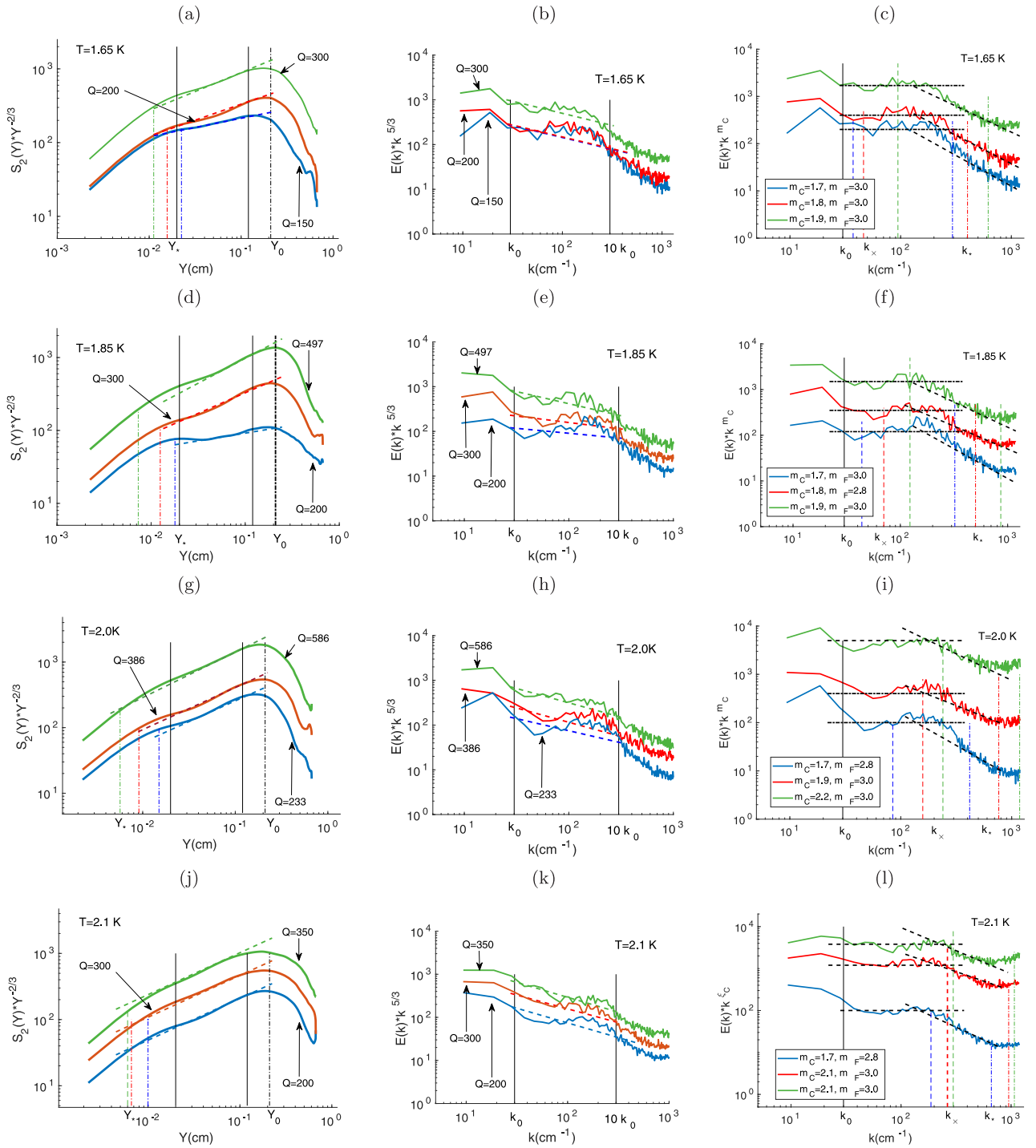
FIG. 1. The second-order statistics for different T and heat fluxes Q. The figures in the rows (top to down) correspond to $T = 1.65$, 1.85, 2.0, and 2.1 K, respectively. Left column: The second-order structure functions, compensated by K41 scaling, $Y^{-2/3}S_2(Y)$. The colored thin straight lines denote fits with exponents n (cf. Table I, column 13). The fitting range (according to Ref. [13]) is denoted by black vertical thin lines. The black vertical dot-dashed line marks the outer scale of turbulence, denoted as Y_0. The colored vertical dot-dashed line (collectively marked as Y_*) denotes the scales, corresponding to the respective crossover wave numbers k_*. Middle column: the energy spectra compensated by K41 scaling $k^{5/3}E(k)$. Dashed lines of matching colors denote fits $E(k) \propto k^{-\langle m \rangle_{10}}$ in the wave-number interval $k \in [k_0 - 10\,k_0]$, shown by black vertical lines. Right column: the energy spectra, compensated by an individual scaling, $k^{m_C}E(k)$, found by fitting each spectrum in the cascade-dominated range. The compensation is emphasized by horizontal dot-dashed lines. The fits of the mutual-friction-dominated range, $E(k) \propto k^{-m_F}$, are shown by black dashed lines. The vertical lines, corresponding to the crossover wave numbers $k_\times$ (dashed lines) and k_* (dot-dashed lines), are marked in the same color as the corresponding spectra. The legend indicates the scaling exponents m_C for the cascade-dominated range and m_F for the mutual-friction-dominated range. The outer scale of turbulence $k_0 = 2\pi/Y_0$ is marked as a black solid thin line. Different heat fluxes Q (in mW/cm²) are color coded: green, red, and blue lines denote the largest, the intermediate, and the smallest Q, respectively. The color code is the same in all panels.
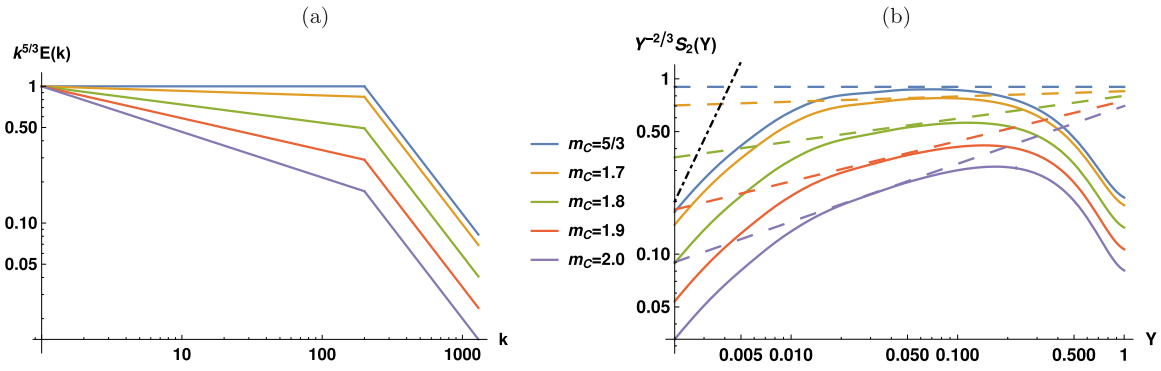
FIG. 2. (a) Piecewise-linear model of the energy spectra $E(k) \propto k^{-m_C}$ for $k < k_\times$ in the cascade-dominated interval and $E(k) \propto k^{-m_F}$, $m_F = 3$ in the mutual-friction-dominated and (b) structure functions $S_2(Y)$, computed using Eq. (7d). The dashed lines of the matching colors correspond to Y^{m_C-1}. The black dot-dashed line corresponds to Y^2.

(i.e., differ only by numerical prefactors). If the angular distribution of energy is not symmetric, the behavior of different energy spectra will differ.

B. A different way of statistical analysis of the visualization data

As we mentioned, the visualization technique allows one to measure the streamwise velocity across a channel as a function of a wall-normal coordinate y for fixed values of the time t_0 and the spanwise and streamwise positions z_0 and x_0,

$$u(y) \equiv u_x(x_0, y, z_0, t_0). \tag{6}$$

For simplicity, we choose $t_0 = 0$ and $z_0 = x_0 = 0$, i.e., $u_x(0, y, 0, 0)$.

So far, the way to statistically analyze the data, i.e., Eq. (6), was to find the velocity differences $\Delta u_x(Y, y, t)$ defined in Eq. (1b) and calculate the structure functions $S_n(Y)$ using Eqs. (1a) and (1c). The theoretical analysis of homogeneous turbulence is traditionally done in the Fourier space, where different Fourier components are statistically independent: $\langle v^\alpha(\boldsymbol{k}) v^\beta(\boldsymbol{k}') \rangle = 0$ if $\boldsymbol{k} \neq \boldsymbol{k}'$. We will demonstrate in this paper that a similar approach (in the k_y space) to the data analysis of the visualization data allows one to get additional information on the statistics of counterflow turbulence that is hidden in the approach based on $S_2(\delta)$.

To this end, we define a 1D Fourier transform $v(k_y)$ similar to its 3D version given by Eq. (3b):

$$v(k_y) = \int_{-D/2}^{D/2} u(y) \exp(i k_y y) dy. \tag{7a}$$

Here, $y = 0$ is the position of the centerline and D is the channel width. Similarly to Eq. (3a), we define next the 1D energy spectrum,

$$2\pi \, \delta(k_y + k_y') E(k_y) = \langle v(k_y) v(k_y') \rangle, \tag{7b}$$

which is simply $E_{xz}(k_y)$, defined by Eq. (4c). To see this, notice that integration over $dk_x/(2\pi)$ and $dk_z/(2\pi)$ in Eq. (4c), according to Eq. (3c), results in $\boldsymbol{u}_i(x = 0, y, z = 0)$.

Our expectation is that $v(k_y)$ [and, respectively, $E(k_y)$] better separates turbulent fluctuations with different scales than $\Delta u(Y, y)$ [and, respectively, $S_2(Y)$]. To see this, one may consider the relation between $E(k_y)$ and $S_2(Y)$. Using the inverse Fourier transform of Eq. (7a),

$$u(y) = \int v(k_y) \exp(-i k_y y) \, dy, \tag{7c}$$

in the definition of $S_2(Y)$ [i.e., Eq. (1a)] and applying Eq. (7b), one gets

$$S_2(Y) = \frac{2}{\pi} \int \sin^2\left(\frac{k_y Y}{2}\right) E_{xz}(k_y) \, dk_y. \tag{7d}$$
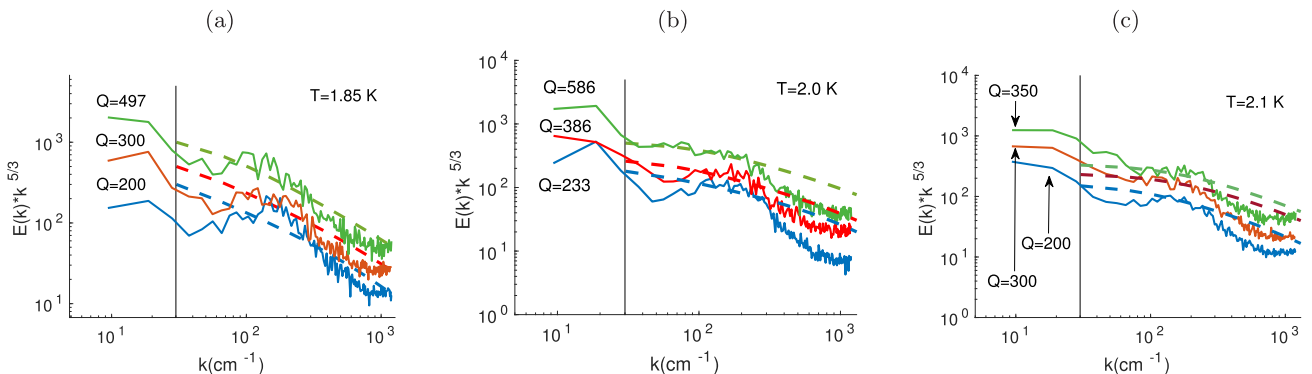

FIG. 3. Comparison of the experimental compensated energy spectra $k^{5/3} E(k)$ with the theoretical predictions [17] (dashed lines) for different temperatures T K and heat fluxes Q (in mW/s^2). Vertical solid lines denote the outer scale k_0.
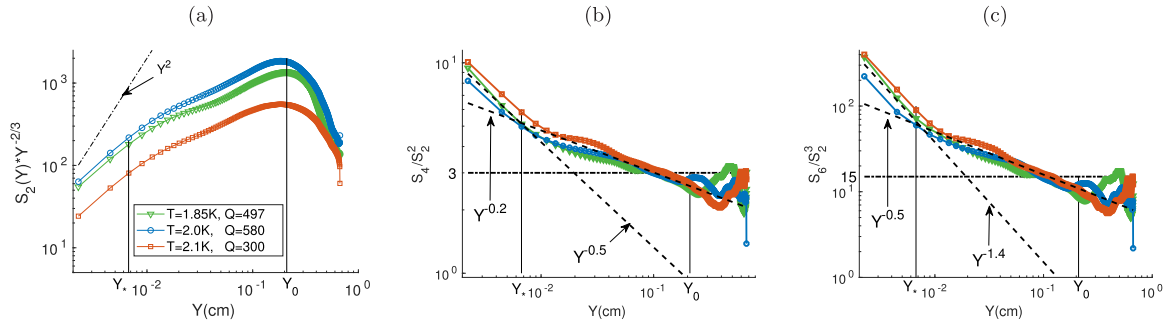
FIG. 4. Second- and higher-order statistics at different temperatures. The flow parameters are shown in the legend of (a). (a) The structure functions $S_2(Y)$. The dot-dashed black line denotes the asymptotic viscous behavior for $S_2(Y) \propto Y^2$. (b) Flatness $F_4(Y) = S_4(Y)/S_2^2(Y)$. (c) Hyperflatness $F_6(Y) = S_6(Y)/S_2^3(Y)$. The horizontal dot-dashed lines in (b) and (c) denote the Gaussian values of $F_4(Y)$ and $F_6(Y)$. The approximate Y dependencies of the flatness and hyperflatness for $Y \gtrsim Y_*$ are shown by dashed lines, marked $Y^{-0.2}$ and $Y^{-0.5}$, respectively. These values are slightly larger than typical for the classical hydrodynamic turbulence, i.e., $\delta^{-0.14}$ and $\delta^{-0.38}$ in Ref. [27]. However, for $Y \lesssim Y_*$, the effective slopes of $F_4(Y)$ and $F_6(Y)$ strongly increase and become much larger than the classical values; see the dashed lines marked as $Y^{-0.5}$ and $Y^{-1.4}$, respectively. The vertical thin lines in all panels denote positions of the outer scale Y_0 and the crossover scale Y_*.

If this integral converges, it is dominated by the range $k \sim 1/Y$. Therefore, for the infinite extent of the inertial interval, $S_2(Y) \sim F_2(1/Y)Y^{-1}$. For example, if $F(k) \propto k^{-m}$, then $S_2(Y) \propto Y^n$ with $n = m - 1$. It is important to note that the integral in Eq. (7d) also has a contribution from a wide range of k around $1/Y$. Therefore, in a realistic situation with a finite extent of available k space, the relation between $F_n(k_y)$ and $S_n(Y)$ is not so simple.

In any case, as one expects and we demonstrate in this paper, that direct measurement of the *integrand* $E_{xz}(k_y)$ gives more detailed information about the statistics of counterflow turbulence than the measurements of the *integral* [Eq. (7d)] for $S_2(Y)$.

C. Overview of the theory of counterflow turbulence

Analytical theory of counterflow superfluid turbulence, developed in Ref. [17], describes the energy spectra of the normal-fluid and superfluid components of superfluid ^{4}He at scales r exceeding intervortex distance $\ell = 1/\sqrt{\mathcal{L}}$, where $\mathcal{L}$ is the vortex density, i.e., total length of vortex lines per unit volume. The theory is based on the gradually damped version [20] of the coarse-grained Hall-Vinen-Bekarevich-Khalatnikov (HVBK) equations, generalized in Ref. [21] for the counterflow turbulence. These equations have a form of two Navier-Stokes equations for the turbulent velocity fluctuations $\boldsymbol{u}_{\mathrm{n}}(\boldsymbol{r}, t)$ and $\boldsymbol{u}_{\mathrm{s}}(\boldsymbol{r}, t)$, coupled by a simplified version of the mutual-friction force [22],

$$\boldsymbol{f}_{\mathrm{ns}} \simeq \Omega_{\mathrm{s}}[\boldsymbol{u}_{\mathrm{n}}(\boldsymbol{r}, t) - \boldsymbol{u}_{\mathrm{s}}(\boldsymbol{r}, t)], \quad \Omega_{\mathrm{s}} = \alpha(T)\kappa\mathcal{L}. \quad (8)$$

Here, $\alpha(T)$ is the temperature-dependent parameter of the mutual friction, listed in Table I, column 3.

These equations served as a starting point for the derivation of the stationary balance equations for the 1D energy spectra $E_{\mathrm{n}}(k)$ and $E_{\mathrm{s}}(k)$ of the normal and superfluid components,

$$\frac{d\varepsilon_j(k)}{dk} = \Omega_j[E_{\mathrm{ns}}(k) - E_j(k)] - 2\nu_j k^2 E_j(k), \quad (9)$$

using a simplifying assumption of the spatial homogeneity and isotropy of the counterflow turbulence statistics. Here, $\varepsilon_j(k)$ is the energy flux over scales $1/k$ in the normal-fluid

($j = \mathrm{n}$) and superfluid ($j = \mathrm{s}$) velocity components, $\Omega_{\mathrm{n}} = \Omega_{\mathrm{s}}\rho_{\mathrm{s}}/\rho_{\mathrm{n}}$, ν_{n} is the normal-fluid kinematic viscosity (normalized by the ρ_{n}), and ν_{s} is the Vinen's effective superfluid viscosity [5]. The viscouslike energy sink term was added to HVBK equations in Ref. [20] to account for the energy dissipation at the intervortex scale ℓ due to vortex reconnections, the energy transfer to Kelvin waves, and similar effects. In Eq. (9), $E_{\mathrm{n}}(k)$ and $E_{\mathrm{s}}(k)$ are the 1D spherically averaged energy spectra [cf. Eq. (4a)] of the normal-fluid and superfluid subsystems and the cross-correlation function $E_{\mathrm{ns}}(k)$ is related similarly to $F_{\mathrm{ns}}(\boldsymbol{k})$.

Equations (9) are exact (in the framework of HVBK equations), but not closed. To make them practically useful, the closure approximations for $\varepsilon_j(k)$ in terms of $E_j(k)$ were used.

The role of long-range (in the k space) energy-transfer terms was analyzed [17], based on the integral closure for $\varepsilon(k)$ [23], and a new self-consistent closure was suggested:

$$\varepsilon(k) = C(k)k^{5/2}E^{3/2}(k), \quad C(k) = \frac{4C}{3[3 - m(k)]}, \quad (10a)$$

in which $m(k)$ should be understood as a local scaling exponent of $E(k)$,

$$m(k) = \frac{d \ln E(k)}{d \ln(k)}, \quad (10b)$$

and the prefactor $C(k)$ is chosen to reproduce the Kolmogorov constant C for the K41 scaling exponent $m(k) = 5/3$.

To complete the closure of Eqs. (9), the closure [21] for the cross-correlation function E_{ns} was adopted. In a simplified form, suitable for conditions of the visualization experiments [13,14], it reads

$$E_{\mathrm{ns}}(k) = D(k)E_{\mathrm{ns}}^{(0)}(k), \quad D(k) = \frac{\arctan[\xi(k)]}{\xi(k)}, \quad (11a)$$

$$\xi(k) = \frac{k}{k_\times}, \quad k_\times = \frac{\Omega_{\mathrm{ns}}}{U_{\mathrm{ns}}}, \quad \Omega_{\mathrm{ns}} = \Omega_{\mathrm{n}} + \Omega_{\mathrm{s}} = \alpha\kappa\mathcal{L}\frac{\rho}{\rho_{\mathrm{n}}}, \quad (11b)$$

$$E_{\mathrm{ns}}^{(0)}(k) = [\rho_{\mathrm{n}}E_{\mathrm{n}}(k) + \rho_{\mathrm{s}}E_{\mathrm{s}}(k)]/\rho. \quad (11c)$$

TABLE I. Columns 1–3: the temperature and temperature-dependent material parameters of ^{4}He. Columns 4–7: the experimental parameters of the flow. Column 8: the estimates of the normal-fluid Reynolds number, defined by Eq. (14b). Columns 7–12: the estimates of the characteristic wave numbers $k_\times$, k_ν, k_*, and k_ℓ; cf. Sec. III B. Column 13: the estimates of the scaling exponents of the energy spectra via apparent scaling exponents of $S_2(Y)$. Column 14: the mean-over-decade scaling exponents of the energy spectra $\langle m \rangle_{10}$. Columns 15 and 16: the apparent scaling exponents of the energy spectra in the cascade-dominated subinterval m_C and in the mutual-friction-dominated subinterval m_F.

1	2	3	4	5	6	7	8	9	10	11	12	13	14	15	16
T, K	$\frac{\rho_n}{\rho}$	α	Q, $\frac{mW}{cm^2}$	U_n, $\frac{cm}{s}$	U_{ns}, $\frac{cm}{s}$	$\mathcal{L}$, $\frac{1}{cm^2}$	Re_n	$k_\times$ $\frac{1}{cm}$	k_ν $\frac{1}{cm}$	k_* $\frac{1}{cm}$	k_ℓ $\frac{1}{cm}$	$n+1$	$\langle m \rangle_{10}$	m_C	m_F
			150	1.87	2.32	86300	37.9	37.2	149	294	1846	1.89	2.00	1.7	3.0
1.65	0.11	0.11	200	2.23	2.76	16200	46.2	58.8	224	402	2529	2.14	2.10	1.8	3.0
			300	3.27	4.04	38200	84.9	94.5	354	618	3883	2.18	2.20	1.9	2.9
			200	1.18	1.85	81100	53.2	43.8	249	322	1788	1.88	1.88	1.7	3.0
1.85	0.19	0.18	300	1.78	2.80	19800	94.2	70.1	539	502	2796	2.23	1.95	1.8	2.8
			497	3.03	4.76	58500	165	123	755	863	4806	2.35	2.20	1.9	2.8
			233	0.86	1.92	14100	84.7	73.3	455	418	2359	2.3	2.20	1.7	3.0
2.00	0.55	0.28	386	1.34	3.00	47300	131	158	690	765	4321	2.31	2.30	1.9	2.8
			586	2.09	4.67	112000	223	240	1102	1178	6650	2.36	2.30	2.2	3.0
			200	0.57	2.20	37300	107	170	588	612	3837	2.30	2.25	1.7	2.9
2.10	0.74	0.48	300	0.88	3.40	89800	159	264	958	951	5951	2.30	2.30	2.1	3.0
			350	0.99	3.83	114000	211	298	1142	1071	6705	2.30	2.35	2.2	3.0

Here, $D(k)$ is the U_{ns}-dependent decoupling function and $E_n(k)$ and $E_s(k)$ are the U_{ns}-dependent energy spectra, found self-consistently by solving Eqs. (9) with $E_{ns}(k)$ given by Eqs. (11).

Further simplification of the balance equations (9)–(11) for the experimental conditions results in decoupled balance equations for the normal-fluid and the superfluid energy spectra,

$$C(k) \frac{d}{dk} k^{5/2} E_j^{3/2}(k) = E_j(k)\{\Omega_j[D(k)-1] - 2\nu_j k^2\}, \quad (12)$$

in which $C(k)$ and $D(k)$ are defined by Eqs. (10a) and (11a). The solutions of these equations are compared with the experimental spectra in Fig. 3.

To summarize this overview, we note that analytical theory [17] describes the main features of the large-scale normal-fluid energy spectra of counterflow turbulence, observed in the visualization experiments, although it does not account for the inhomogeneity and anisotropy of the flow.

III. EXPERIMENTAL RESULTS AND THEIR ANALYSIS

In this section, we analyze the experimental data of the normal-fluid turbulent velocity fluctuations $u(y)$, obtained for $T = 1.65$, 1.85, 2.00, and 2.10 K with three values of heat fluxes Q at each temperature. The main parameters of these experiments are given in Table I. This table also collects the values of important characteristic wave numbers, estimated below in Sec. III B. The second-order statistics [i.e., the structure functions and the spectra $E_{zx}(k_y)$] are discussed in Sec. III C and the higher-order statistics of the structure functions in Sec. III E.

A. Experimental techniques

The experimental apparatus is identical to that described in Refs. [13,14]. A stainless-steel channel of 9.5-mm-square cross section with a total length of 300 mm is attached to a pumped helium bath whose temperature can be controlled within 0.1 mK by regulating the vapor pressure. A planar heater (around 400 Ω) at the lower end of the channel was used to drive a thermal counterflow. When the heat flux is sufficiently large, both the superfluid and the normal-fluid components can become turbulent. To probe the normal-fluid turbulence, our recently developed He$_2^*$ molecular tracer-line tracking technique [24] was adopted. A 35 fs pulsed laser with a repetition rate of 5 kHz and a pulse energy of about 60 μJ was focused into the channel to produce a thin line of He$_2^*$ molecular tracers. This tracer line can be driven to produce 640 nm fluorescent light by a pulse train from an imaging laser at 905 nm (i.e., 5–6 pulses at a repetition rate of 500 Hz). The fluorescence was captured by an intensified CCD (ICCD) camera, mounted perpendicular to both the flow direction and the laser-beam path, to produce the images of the tracer line. In a typical experiment, a straight baseline image is acquired to serve as a reference. Then, the heater is turned on for at least 20 s so that a fully developed counterflow can establish in the channel. After that, we produce a tracer line and let the tracer line move with the normal fluid by a drift time Δt before the drifted line is imaged.

In order to extract quantitative velocity field information, the center location of every line segment needs to be accurately determined. In our previous research [13,14], a simple Gaussian fit method was adopted. First, the image of a tracer line was cut into many small segments (i.e., typically 40–60 segments). Then, the fluorescence intensity profile of each line segment was fit by a Gaussian function such that both the center location and the width of the line segment can be determined. The streamwise velocity of the normal fluid at position y can be calculated as the displacement of the line segment divided by the drift time Δt. This method works well only when the tracer-line image has good quality and high signal-to-noise ratio. However, as the normal-fluid velocity

increases, some line segments can distort and smear, which can result in significant uncertainty in locating the center of these segments using the Gaussian fit method. In this research, we utilized a more sophisticated approach, which is based on the algorithm proposed by Pulkkinen *et al.* for finding curvilinear structures in noisy data [25]. There are two steps involved in the image analysis. First, a tracer-line image is noise filtered based on the intensity of bright pixels using numerically inexpensive nearest-neighbor searches. The basic idea is to remove those bright pixels that are surrounded all by dark pixels and hence are more likely created due to instrument or environmental noises [26]. Subsequently, the algorithm of Ref. [25] is applied to determine the ridge line of the entire fluorescence intensity profile. The displacement of the ridge line then allows us to calculate the streamwise normal-fluid velocity regardless of the bad quality of some local line segments.

Based on the obtained streamwise normal-fluid velocity $u_x(y)$, we can evaluate the velocity difference $\Delta u_x(Y, y) = u_x(y + Y) - u_x(y)$ between two line segments that are separated by a distance Y. Then, the transverse structure functions of the normal-fluid turbulence can be easily computed as $S_n(Y) = \langle |\Delta u_y(y, Y)|^n \rangle$, where the angle brackets $\langle \cdot \rangle$ denote an ensemble average over all the images obtained under the same experimental conditions (typically 30–100 images). The calculated structure function profiles are found to be insensitive to the reference location y. The 1D energy spectra, averaged over the x-z plane and parallel to the channel wall, can also be determined. In Fig. 1, we show the obtained structure function and energy spectra curves at various temperatures and heat fluxes. It should be noted that the results for separation distance Y smaller than the thickness of the tracer line (i.e., about 100–200 μm) can have large uncertainties.

B. Estimates of the crossover wave numbers

1. Decoupling wave number $k_\times$

According to Ref. [21], the decoupling wave number $k_\times$, for which the decoupling function $D(k) = \frac{1}{2}$, is estimated as

$$k_\times \simeq 2\,\Omega_{\mathrm{ns}}/U_{\mathrm{ns}} \simeq \kappa \mathcal{L}/U_{\mathrm{ns}}. \tag{13}$$

For typical values $\mathcal{L} \simeq 10^5\,\mathrm{cm}^{-2}$, $U_{\mathrm{ns}} \simeq 1\,\mathrm{cm/s}$ and with $\kappa \simeq 10^{-3}\,\mathrm{cm}^2/\mathrm{s}$, this gives $k_\times \simeq 100\,\mathrm{cm}^{-1}$. The particular values of $k_\times$ for each of the 12 experimental sets are presented in Table I, column 9.

2. Viscous wave number k_ν

The viscous wave number k_ν, for which the viscous damping becomes comparable with the energy transfer over scales, can be estimated by comparison of the viscous damping frequency νk^2 with the eddy-turnover frequency $\sqrt{k^3 E(k)}$,

$$k_\nu \simeq E(k_\nu)/\nu^2. \tag{14a}$$

Using the K41 estimate for the energy spectrum $E_{\mathrm{K41}}(k) \simeq u_{\mathrm{T}}^2 k_0^{2/3} k^{-5/3}$, we get

$$\frac{k_\nu}{k_0} \simeq \left[\frac{E(k_\nu)}{E_{\mathrm{K41}}(k_\nu)}\right]^{3/8} \mathrm{Re}^{3/4}, \quad \mathrm{Re} = \frac{u_{\mathrm{T}}}{k_0 \nu}. \tag{14b}$$

Here u_{T} is the rms velocity fluctuations and $k_0 \simeq 30\,\mathrm{cm}^{-1}$, estimated in Ref. [13] from the behavior of $S_2(Y)$. Our estimates of k_ν are given in Table I, column 10.

Equation (14b) is a generalization of the well-known K41 relationship $k_\nu \simeq k_0 \mathrm{Re}^{3/4}$ for the spectra that differ significantly from the K41 scaling $E_{\mathrm{K41}}(k) \propto k^{-5/3}$.

3. Mutual friction—viscous crossover wave number k_*

We know that the characteristic frequency responsible for the rate of energy dissipation by mutual friction in the normal-fluid component is $\alpha \dfrac{\rho_{\mathrm{s}}}{\rho_{\mathrm{n}}} \kappa \mathcal{L}$, while the corresponding frequency for the viscous dissipation is $\nu_{\mathrm{n}} k^2$. Comparing these two frequencies, one finds a crossover wave number k_* for which the efficiencies of these two dissipation mechanisms are equal,

$$k_* = \sqrt{\alpha \frac{\rho_{\mathrm{s}}}{\rho_{\mathrm{n}}} \frac{\kappa}{\nu_{\mathrm{n}}} \mathcal{L}}. \tag{15}$$

Substituting the particular temperature-dependent values of α, ρ_{n}, and ν_{n}, we get the values shown in Table I, rows 11. As we see, for $T = 1.65$ and $T = 2.10$ K, $k_* \approx 1.0\,\sqrt{\mathcal{L}}$, while for $T = 1.85$ and $T = 2.00$ K, $k_* \approx 1.1\sqrt{\mathcal{L}}$. This is smaller than the wave number

$$k_\ell \approx 2\pi \sqrt{\mathcal{L}} \tag{16}$$

(cf. Table I, column 12), which separates the quasiclassical and ultraquantum regimes of superfluid turbulence.

C. Second-order statistics of counterflow turbulence

Figure 1 summarizes the second-order statistics of the velocity fluctuations for different temperatures and flow parameters. Both the structure functions (left column) and the 1D energy spectra (middle column) are compensated by the K41 scaling: $Y^{2/3} S_2(Y)$, $k_y^{5/3} E_{xz}(k_y)$. In the right column, we plot the energy spectra compensated in the cascade-dominated range; see below.

1. Second-order structure functions

The structure functions in the counterflow share similarity with the velocity structure functions in the classical hydrodynamic turbulence. The expected inertial interval of scales $\delta_{\min} \approx 0.02$ to $\delta_{\max} \simeq 0.2$ cm are marked by black thin vertical lines and correspond to that in Ref. [13]. Clearly, the structure functions are steeper than their classical counterparts. The apparent scaling behavior in this interval of scales may be characterized by exponents n. These exponents were found in Ref. [13] and are reproduced in Table I, column 13. The values of n for $T = 2.1$ K are slightly larger than in Ref. [13], likely due to the improved image analysis and the fitting procedure. Note that the values of n vary widely, depending on the flow parameters: the temperature and the heat flux.

The dot-dashed vertical lines, colored as the structure functions and collectively marked Y_*, denote the scale that delineates the ranges of dominance of two dissipative mechanisms: the mutual friction (for $Y > Y_*$) and the viscous dissipation (for $Y < Y_*$).

We should also note that simple analysis of Eq. (7d) shows that the small-scale behavior $S_2(Y) \propto Y^2$ appears if the energy spectrum $E(k)$ decays as k^{-3} or faster (including the exponential decay). Therefore, the apparent Y^2 scaling cannot be uniquely connected with the viscous dissipation of turbulent kinetic energy, as in the classical turbulence. Moreover, the asymptotic slope $S_2(Y) \propto Y^2$ at $Y \lesssim Y_*$ is not reached in our experiments due the limited spatial resolution [cf. Fig. 4(a)].

2. Energy spectra of counterflow turbulence

One-dimensional energy spectra, compensated by K41 scaling $k^{5/3}E(k)$, are shown in Fig. 1, middle column. We can easily identify several k ranges with different k dependence of the spectra. The small wave-number ($k \lesssim k_0$) behavior is clearly different from the rest of the spectrum. A relatively short part of the spectra is close to compensation by K41 while remaining steeper. The large-k part of the spectra has a much larger slope, extending over all remaining interval of scales. We will now try to relate between these different types of behavior and various crossover wave numbers introduced in Sec. III B.

(a) Energy-containing interval. The outer scale of turbulence, $k_0 \simeq 30 \text{ cm}^{-1}$, was taken according to Ref. [13], where it was estimated as $2\pi/r_0$ with $r_0 \simeq 0.2 \text{ cm}$ close to the maximum of the structure functions. The positions of k_0 are marked in Fig. 1, middle and right columns, by vertical black thin solid lines. The range $k \lesssim k_0$ can be interpreted as an energy-containing interval, where energy is pumped into the system due to instabilities of mean flow in the channel and in which most of the flow energy is localized. As we see, this value corresponds well to a boundary between the large-scale behavior and the inertial-like scaling behavior of the spectra for large heat fluxes, while for low heat fluxes and low temperature, the energy-containing interval seems to extend to higher wave numbers.

(b) Cascade-dominated interval. The next characteristic scale $k_\times$ (cf. Table I, column 9) estimates the wave number for which the decoupling function $D(k_\times) = \frac{1}{2}$. For $k \lesssim k_\times$, $D(k) > \frac{1}{2}$, and the energy dissipation by the mutual friction is relatively weak. In this k range, the main mechanism responsible for the energy transfer over scales is the Richardson-Kolmogorov energy cascade, similar to that in classical turbulence. Nevertheless, the energy dissipation by the mutual friction cannot be fully ignored. Therefore, the energy spectra in this range of scales are steeper than the K41 scaling, as is clearly seen in Fig. 1, middle column. All these motivate us to name the wave-number range $k_0 \lesssim k \lesssim k_\times$ as *cascade-dominated interval*.

It was suggested in Ref. [17] to characterize the apparent scaling of the otherwise non-scale-invariant spectra by calculating a mean exponent over some interval of scales. The theoretical mean exponents over a first decade $\langle m \rangle_{10}$ were found to agree with the experimental exponents [13] of the structure functions [17]. We calculate the mean exponents over a k range $k \in [30\text{–}300]$ (a decade in k/k_0) and collect them in Table I, column 14. These values are close to $n + 1$, where n is the apparent scaling exponent of $S_2(Y) \propto Y^n$, defined by Eq. (7d). This means that the idea to estimate $\langle m \rangle_{10}$

via $n + 1$ indeed works reasonably well. The corresponding fits are shown in Fig. 1, middle column, as dashed colored lines. However, although the values of the mean exponents agree with the scaling of the structure functions, the actual scaling of the spectra is different.

To estimate the apparent scaling exponents m_c of the energy spectra $E(k) \propto k^{-m_c}$ in the cascade-dominated interval, we plot the experimental spectra, compensated by k^{m_c}, and choose the value of m_c so as to maximize the k range where $k^{m_c}E(k) \approx$ const. The resulting plots are shown in Fig. 1, right column, where the crossover scales $k_\times$ are shown by vertical dashed colored lines. It is remarkable that except for the low heat fluxes at $T = 1.65$ and 1.85 K, the crossover between different scaling regimes of the energy spectra coincides well with $k_\times$.

(c) Mutual-friction-dominated interval. For $k \gtrsim k_\times$, where the decoupling function is small and mutual friction becomes important in the energy balance [17], the slope of the energy spectra increases significantly from $m_c \approx 2.0 \pm 0.2$ to $m_F \approx 2.9 \pm 0.1$. The transition between the two types of behavior is not sharp, especially for low-heat fluxes, but clearly visible.

The power-law-like behavior $E(k) \propto k^{-m_F}$ qualitatively differs from the exponential decay of $E(k)$, typical for the viscous interval of k in the classical hydrodynamic turbulence. Therefore, we consider this behavior as an evidence that for $k \gtrsim k_\times$, the main mechanism of the energy dissipation is the mutual friction. Upper limits of the mutual-friction-dominated interval k_* are shown in Fig. 1, right column, by vertical dot-dashed lines of the corresponding colors. As a rule, the values of k_* are about or above the largest available values of k. This means that the viscous interval of wave numbers is beyond our spectral resolution. The corresponding Y_* are shown in Fig. 1, left column, and are mostly smaller than the implied boundary between the inertial and viscous behavior [13] (i.e., black vertical thin solid lines). Therefore, only at the smallest scales does the viscous dissipation become important, but it is still not dominant, as we show below.

3. More about connection between $S_2(Y)$ and $E(k)$

To clarify the relation between the energy spectra in a finite k range and the structure functions, we plot in Fig. 2(a) a piecewise-linear model of the energy spectra, consisting of $E(k) = k^{-m_c}$ in the cascade-dominated interval $k_0 < k < k_\times$, continuously connected with the $E(k) \propto k^{-m_F}$ part in the mutual-friction-dominated interval $k_\times < k < k_*$. We used the typical values of m_c, and the same values of $m_F = 3.0$, $k_\times = 200 \text{ cm}^{-1}$, and $k_* = 1300$ for all spectra. For simplicity, we adopt for the energy-containing interval the same behavior $E(k) = k^{-m_c}$ as in the cascade-dominated interval. The structure functions, computed using Eq. (7d), are shown in Fig. 2(b) together with the expected slope $S_2(Y) \propto Y^n$ with $n = m_c - 1$, shown by the dashed lines. As we see, the actual range of scales, over which the original scaling is recovered, is very narrow.

The slope $S_2(Y) \propto Y^2$, typical for viscous exponential decay of $E(k)$ in the classical hydrodynamic turbulence, and $E(k) \propto k^{-3}$, typical for the mutual-friction-dominated interval in counterflow turbulence, are shown by a black

dot-dashed line. As expected, for the finite-scaling interval of a modest extent, the resulting Y dependence of $S_2(Y)$ demonstrates a very smooth transition between these regimes and does not reach the genuine asymptotic behavior $S_2(Y) \propto Y^2$.

D. Comparison of analytically predicted and experimental energy spectra

It is instructive to directly compare the experimental spectra with the spectra predicted by theory [17]. The theory does not describe the largest scales motion in the energy-containing interval (for $k < k_0$) and has the energy influx for $k = k_0$ [or the boundary condition $E_0 = E^{\text{th}}(k_0)$] as an external parameter of the theory.

The theory was developed for an idealized situation of fully developed, space-homogeneous turbulence. Naturally, the real physical situation in the experiments (i.e., wall-bounded, spatially inhomogeneous channel flow for relatively low Reynolds numbers) is more complicated than assumed by the theory. Therefore, the comparison is meaningful only for the experiment with relevant flow conditions. In our case, we may take the $\text{Re}_n > 100$ as a tentative criterion for the well-developed turbulence in the channel. This leaves out the low-temperature data ($T = 1.65$ K), as well as the lowest heat fluxes for $T = 1.85$ and 2.0 K. However, we keep for completeness all the data for $T = 1.85$ and 2.0 K.

In Fig. 3, we compare the experimental (K41-compensated) energy spectra for $T = 1.85$, 2.0, and 2.1 K (plotted as solid colored lines) with the predicted energy spectra (denoted by dashed lines of the same color), calculated for the same temperatures and the same heat fluxes. The theoretical spectra were made dimensional and $E^{\text{th}}(k_0)$ was taken to ensure overlap in the cascade-dominated k range. For high-heat fluxes, these values agree well with $E^{\text{exp}}(k_0)$.

The immediate observation is a qualitative agreement between the experimental and theoretical spectra over a large range of wave numbers, covering most of the cascade-dominated range. The deviations are mostly limited to the spectra with the lowest-heat fluxes for $T = 2.0$ and $T = 2.1$ K. At $T = 1.85$ K, the agreement is recovered for wave numbers larger than k_0, which may indicate that the turbulence in these experiments is not yet fully developed and the outer scale is smaller than expected.

As mentioned above, the overall suppression of the spectra compared to the classical behavior is well captured by the mean scaling exponents $\langle m \rangle_{10}$; cf. Table I, column 14.

On the other hand, the theory does not describe the sharp drop of the spectra in the mutual-friction-dominated k range, demonstrating only smooth decrease of the current slope $m(k)$ of the spectra for large k. A possible reason is that the theory [17] does not take into account the energy exchange between components that is most efficient in this range of scale. Other flow conditions, which are not accounted for by the theory, may contribute to this discrepancy. Also the experimental data in the high-k regime may not be very reliable indeed. This is because the corresponding separation scale is comparable or even smaller than the width of the tracer line, which leads to large uncertainty.

E. Flatness, hyperflatness, and intermittency

To analyze higher-order statistics and possible intermittency effects, we select one example at each temperature, having similar Y_*, and plot in Fig. 4 the structure functions $Y^{-2/3} S_2(Y)$, the flatness $F_4(Y) = S_4(Y)/S_2^2(Y)$, and the hyperflatness $F_6(Y) = S_6(Y)/S_2^3(Y)$.

In all panels, we mark the positions of the outer scale of turbulence Y_0 and the crossover scale Y_*. As is clearly seen in Fig. 4(a), the asymptotic behavior Y^2 is not reached with our spatial resolution. However, Y_* delineates different types of behavior of the $S_2(Y)$. These different regimes are even better exhibited by flatness and hyperflatness in Figs. 4(b) and 4(c).

For Gaussian statistics, $F_4 = 3$ and $F_6 = 15$, shown in Figs. 4(b) and 4(c) as horizontal dashed lines. Clearly, for large scales $Y \gtrsim Y_0$, $F_4(Y)$ and $F_6(Y)$ are close to the Gaussian values, indicating that the statistics of the turbulent velocity field in the energy-containing interval is indeed close to Gaussian. This is a common property of classical hydrodynamic turbulence, independent of the way of its excitation.

In a wide interval of scales $Y_* \lesssim Y \lesssim Y_0$, covering scales corresponding to both the cascade-dominated and mutual-friction-dominated spectral ranges, both $F_4(Y)$ [Fig. 4(b)] and $F_6(Y)$ [Fig. 4(c)] have a power-law-like behavior $F_n(Y) \propto Y^{-x_n^{(1)}}$, with exponents $x_4^{(1)} \simeq 0.20 \pm 0.02$ and $x_6^{(1)} \simeq 0.5 \pm 0.03$. To compare these exponents with their counterparts x_n^{HT} in the classical hydrodynamic turbulence, recall that $x_n^{\text{HT}} = \zeta_n^{\text{HT}} - n\zeta_2^{\text{HT}}/2$, where ζ_n^{HT} is the scaling exponent of the n-order structure function in classical hydrodynamic turbulence. With the most recent experimental values [27] $\zeta_2^{\text{HT}} \approx 0.72$, $\zeta_4^{\text{HT}} \approx 1.30$, and $\zeta_6^{\text{HT}} \approx 1.78$, this gives $x_4^{\text{HT}} \approx 0.14$ and $x_6^{\text{HT}} \approx 0.38$. We conclude that the values $x_{4,6}^{(1)}$ are moderately, but distinctly, larger than ζ_n^{HT}. Notably, the structure functions and higher-order statistics are not sensitive to the peculiarities of the energy spectra, in particular to the existence of two significantly different scaling ranges.

However, at smaller scales $Y \lesssim Y_*$, the effective slopes of $F_4(Y)$ and $F_6(Y)$ increase dramatically. The estimates, shown in Figs. 4(b) and 4(c), give $x_4^{(2)} \simeq 0.5 \pm 0.1$ and $x_6^{(2)} \simeq 1.4 \pm 0.1$ at these scales, which correspond to the dissipative range with mixed contributions of the mutual-friction and viscous dissipations. The statistics become very intermittent. The fact that we do not observe saturation of $F_4(Y)$ and $F_6(Y)$, typical for the viscous range in the classical turbulence, supports our conjecture that the viscous dissipation-dominant range is beyond our resolution.

IV. CONCLUSION

In this paper, we report a detailed analysis of the energy spectra, second- and high-order structure functions of velocity differences in the superfluid ^{4}He counterflow turbulence, measured in a wide range of temperatures and heat fluxes. In particular, we discover two ranges of wave numbers k_y with very different apparent exponents of the one-dimensional energy spectra in the cascade-dominated (for relatively small k_y) and the mutual-friction-dominated subintervals (for relatively large k_y), respectively. The general behavior of the

experimental spectra $E_{xz}(k_y)$ in the cascade-dominated range agrees well with the energy spectra, predicted in Ref. [17].

The analysis of the statistics of the high-order structure functions shows that in the energy-containing interval, the statistics of counterflow turbulence is close to Gaussian, similar to the classical hydrodynamic turbulence. In the cascade- and mutual-friction-dominated intervals, we found some modest enhancement of intermittency with respect to its level in classical turbulence. However, at small scales (but not yet viscous scales), the intermittency becomes much stronger than that in the classical turbulence.

In conclusion, we should remember that the theory, developed in Ref. [17], does not describe the experimental observations reported here in all details. Besides the obvious reason of spatial inhomogeneity, especially important for modest available Reynolds numbers Re_n, there is one more possible reason for some disagreement even in the $Re_n \to \infty$ limit. This is the anisotropy of statistics of counterflow turbulence. Although we do not yet have experimental information regarding how strong the anisotropy of turbulent statistics is, this effect is definitely there due to presence of preferred $\boldsymbol{U}_{ns}$ direction and strong dependence of the cross-correlation function $E_{ns}(\boldsymbol{k})$ (between the normal-fluid and superfluid velocity components) on the angle between $\boldsymbol{U}_{ns}$ and $\boldsymbol{k}$, predicted in Ref. [21]. The study of the effect of anisotropy on the statistics of counterflow turbulence is on our nearest agenda. Nevertheless, the reasonable agreement between our observations and the theory [17] is encouraging. In particular, the crossover scales between different regimes, predicted by the theory using macroscopic parameters of the flow and clearly observed in the spectra and structure functions, make us believe that what we know so far contains an essential part of the basic physics of the problem.

[1] R. J. Donnelly and C. F. Barenghi, The observed properties of liquid helium at the saturated vapor pressure, J. Phys. Chem. Ref. Data **27**, 1217 (1998).

[2] R. J. Donnelly, *Quantized Vortices in Hellium II* (Cambridge University Press, Cambridge, 1991).

[3] *Quantized Vortex Dynamics and Superfluid Turbulence*, edited by C. F. Barenghi, R. J. Donnelly, and W. F. Vinen, Lect. Notes Phys. Vol. 571 (Springer-Verlag, Berlin, 2001).

[4] R. P. Feynman, Application of quantum mechanics to liquid helium, Prog. Low Temp. Phys. **1**, 17 (1955).

[5] W. F. Vinen and J. J. Niemela, Quantum Turbulence, J. Low Temp. Phys. **128**, 167 (2002).

[6] H. E. Hall and W. F. Vinen, The rotation of liquid helium II. I. Experiments on the propagation of second sound in uniformly rotating helium II, Proc. R. Soc. A **238**, 204 (1956).

[7] W. F. Vinen, Mutual friction in a heat current in liquid helium II I. Experiments on steady heat currents, Proc. R. Soc. **240**, 114 (1957); Mutual friction in a heat current in liquid helium II. II. Experiments on transient effects, **240**, 128 (1957); Mutual friction in a heat current in liquid helium II III. Theory of the mutual friction, **242**, 493 (1957); Mutual friction in a heat current in liquid helium. II. IV. Critical heat currents in wide channels, **243**, 400 (1958).

[8] R. N. Hills and P. H. Roberts, Superfluid mechanics for a high density of vortex lines, Arch. Ration. Mech. Anal. **66**, 43 (1977).

[9] L. Skrbek and K. R. Sreenivasan, How similar is quantum turbulence to classical turbulence, in *Ten Chapters in Turbulence*, edited by P. A. Davidson, Y. Kaneda, and K. R. Sreenivasan (Cambridge University Press, Cambridge, 2013), pp. 405–437.

[10] C. F. Barenghi, V. S. L'vov, and P.-E. Roche, Experimental, numerical, and analytical velocity spectra in turbulent quantum fluid, Proc. Natl. Acad. Sci. USA **111**, 4683 (2014).

[11] E. Rusaouen, B. Chabaud, J. Salort, and P.-E. Roche, Intermittency of quantum turbulence with superfluid fractions from 0% to 96%, Phys. Fluids **29**, 105108 (2017).

[12] L. Skrbek and K. R. Sreenivasan, Developed quantum turbulence and its decay, Phys. Fluids **24**, 011301 (2012).

[13] J. Gao, E. Varga, W. Guo, and W. F. Vinen, Energy spectrum of thermal counterflow turbulence in superfluid helium-4, Phys. Rev. B **96**, 094511 (2017).

[14] A. Marakov, J. Gao, W. Guo, S. W. Van Sciver, G. G. Ihas, D. N. McKinsey, and W. F. Vinen, Visualization of the normal-fluid turbulence in counterflowing superfluid ^{4}He, Phys. Rev. B **91**, 094503 (2015).

[15] M. La Mantia, P. Švančara, D. Duda, and L. Skrbek, Small-scale universality of particle dynamics in quantum turbulence, Phys. Rev. B **94**, 184512 (2016).

[16] M. La Mantia, Particle dynamics in wall-bounded thermal counterflow of superfluid helium, Phys. Fluids **29**, 065102 (2017).

[17] V. S. L'vov and A. Pomyalov, Theory of energy spectra in superfluid ^{4}He counterflow turbulence, Phys. Rev. B **97**, 214513 (2018).

[18] L. Biferale, D. Khomenko, V. L'vov, A. Pomyalov, I. Procaccia, and G. Sahoo, Turbulent statistics and intermittency enhancement in coflowing superfluid ^{4}He, Phys. Rev. Fluids **3**, 024605 (2018).

[19] E. Varga, J. Gao, W. Guo, and L. Skrbek, Intermittency enhancement in quantum turbulence in superfluid ^{4}He, Phys. Rev. Fluids **3**, 094601 (2018).

[20] L. Boué, V. S. L'vov, Y. Nagar, S. V. Nazarenko, A. Pomyalov, and I. Procaccia, Energy and vorticity spectra in turbulent superfluid ^{4}He from $T = 0$ to T_λ, Phys. Rev. B **91**, 144501 (2015).

[21] D. Khomenko, V. S. L'vov, A. Pomyalov, and I. Procaccia, Counterflow induced decoupling in superfluid turbulence, Phys. Rev. B **93**, 014516 (2016).

[22] V. S. L'vov, S. V. Nazarenko and G. E. Volovik, Energy spectra of developed superfluid turbulence, JETP Lett. **80**, 479 (2004).

[23] V. S. L'vov, S. V. Nazarenko, and O. Rudenko, Bottleneck crossover between classical and quantumsuperfluid turbulence, Phys. Rev. B **76**, 024520 (2007).

[24] J. Gao, A. Marakov, W. Guo, B. T. Pawlowski, S. W. Van Sciver, G. G. Ihas, D. N. McKinsey, and W. F. Vinen, Producing and imaging a thin line of He_2^* tracer molecules in helium-4, Rev. Sci. Instrum. **86**, 093904 (2015).

[25] S. Pulkkinen, M. M. Mäkelä and N. Karmitsa, A generative model and a generalized trust region newton method for noise reduction, Comput. Optim. Appl. **57**, 129 (2014).

[26] M. Piccardi, Background subtraction techniques: A review, in *2004 IEEE International Conference on Systems, Man and Cybernetics*, IEEE Cat. No. 04CH37583 (IEEE, The Hague, 2004).

[27] K. P. Iyer, K. R. Sreenivasan, and P. K. Yeung, Reynolds number scaling of velocity increments in isotropic turbulence, Phys. Rev. E **95**, 021101 (2017).